

# Effects of Cu Content and Preaging on Precipitation Characteristics in Aluminum Alloy 6022

W.F. MIAO and D.E. LAUGHLIN

Effects of Cu content and preaging treatments on precipitation sequence and artificial aging response in aluminum alloy 6022 were investigated using transmission electron microscopy (TEM), differential scanning calorimetry (DSC), and hardness tests. It was found that Cu induces the formation of  $Q$  and its precursor metastable phases and has a beneficial effect on the kinetics of artificial aging. For the alloy with 0.07 wt pct Cu, the precipitation sequence is GP zones  $\rightarrow$  needlelike  $\beta'' \rightarrow$  rodlike  $\beta' +$  lathlike  $Q' \rightarrow \beta +$  Si. On the other hand, the precipitation sequence in the alloy with 0.91 wt pct Cu is GP zones  $\rightarrow$  needlelike  $\beta'' \rightarrow$  lathlike  $Q' \rightarrow Q +$  Si. For the artificial aging condition of 20 minutes at 175 °C, which is the typical automotive paint bake condition, suitable preaging treatments were found to significantly reduce the detrimental effect of the natural aging on artificial aging response.

## I. INTRODUCTION

HEAT treatable (age hardenable) Al-Mg-Si(-Cu) alloys are an important group of aluminum alloys that can be strengthened through precipitation of several metastable phases. The understanding and control of precipitation during artificial aging is therefore critical for achieving optimal properties. Although the precipitation sequence has been studied extensively, not all details in the sequence are clear. Nevertheless, it is generally agreed that the precipitation process in Al-Mg-Si alloys can be roughly divided into the following steps:<sup>[1-4]</sup>



where  $\alpha$  (sss) is the supersaturated solid solution, and GP zones (also called clusters by some authors) are believed to be spherical with uncertain structure. The  $\beta''$  term represents fine needle-shaped precipitates along  $\langle 100 \rangle_{\text{Al}}$ , with a monoclinic structure (different values of the lattice parameters were reported.<sup>[5,6,7]</sup>). The  $\beta'$  term represents rodlike precipitates (circular cross sections) along  $\langle 100 \rangle_{\text{Al}}$ , having a hexagonal crystal structure with  $a = 0.705$  nm and  $c = 0.405$  nm.<sup>[2,8]</sup> However, other lattice parameters for  $\beta'$  have also been reported.<sup>[9]</sup> The  $\beta$  phase ( $\text{Mg}_2\text{Si}$ ) is usually formed as platelets on  $\{100\}$  of Al having the  $\text{CaF}_2$  structure with  $a = 0.639$  nm.<sup>[8]</sup>

The effect of Cu on the precipitation sequence of Al-Mg-Si has also been previously investigated, albeit less extensively. It has been found that the addition of Cu usually enhances the precipitation hardening kinetics.<sup>[10-15]</sup> While some of the investigators attribute this to the refinement in microstructure,<sup>[10,11,12]</sup> others argue that the presence of Cu could also change the precipitation sequence.<sup>[13,14,15]</sup> Apart from the aforementioned precipitates in Al-Mg-Si alloys, Cu-containing precipitates such as  $\theta$  and its precursor metastable phases,<sup>[14]</sup> as well as  $Q$  and its precursor metastable phases,<sup>[15]</sup> could also appear in the precipitation sequence

of Al-Mg-Si-Cu alloys. While  $\theta$  is body-centered tetragonal  $\text{Al}_2\text{Cu}$  with the lattice parameter of  $a = b = 0.607$  nm and  $c = 0.487$  nm,<sup>[16]</sup> the composition of  $Q$  is not determined, although its structure has been proposed to be hexagonal with  $a = 1.04$  nm and  $c = 0.405$  nm.<sup>[17]</sup>

From a more practical point of view, the use of Al-Mg-Si(-Cu) alloys as automotive panel materials is presently increasing,<sup>[18,19]</sup> due to demands for lighter vehicles as part of the overall goal to improve fuel efficiencies and reduce vehicle emissions. The basic requirement for automotive panel materials is high strength and good formability. Although the current emphasis in automotive panel aluminum alloys is to improve the formability at the existing level of strength, strengthening cannot be ignored completely. The strengthening of Al-Mg-Si(-Cu) alloys in automotive applications is usually realized through precipitation hardening occurring during the paint bake cycle with an average temperature of 175 °C and typical duration of about 20 minutes. Unfortunately, the paint bake cycle always produces an underaged condition. In addition, for most Al-Mg-Si(-Cu) alloys, the hardening response during artificial aging is adversely affected by natural aging, *i.e.*, the practically unavoidable delay between solution treatment and artificial aging.<sup>[19,20,21]</sup> In other words, natural aging usually has a deleterious effect on both formability during stamping and strength after the paint bake cycle.

It is well known that the thermal history prior to artificial aging can have a marked effect on the artificial aging response of Al-Mg-Si(-Cu) alloys. In particular, the imposition of a preaging procedure, *i.e.*, an aging at an intermediate temperature immediately after solution treatment, has been shown to greatly influence the precipitation hardening behavior.<sup>[18,20-22]</sup> However, depending on factors such as alloy composition, preaging temperature, and time, the effect of preaging may be positive or negative. Furthermore, the understanding of the underlying mechanisms is far from complete.

In this article, we present the results of an investigation of the effects of Cu content and preaging treatments on the precipitation characteristics and age hardening behavior in aluminum alloy 6022.

W.F. MIAO, Postdoctoral Associate, and D.E. LAUGHLIN, Professor, are with the Department of Materials Science and Engineering, Carnegie Mellon University, Pittsburgh, PA 15213-3890.

Manuscript submitted June 17, 1999.

**Table I. Composition of the Alloys**

Alloy	Mg (Wt Pct)	Si (Wt Pct)	Cu (Wt Pct)	Fe (Wt Pct)	Mn (Wt Pct)	Al (Wt Pct)
A	0.58	1.28	0.07	0.11	0.08	balance
B	0.55	1.26	0.91	0.11	0.07	balance

## II. EXPERIMENTAL PROCEDURE

The compositions of the 6022-type alloys used in this study, designated as alloys A and B, respectively, are given in Table I. The main difference between alloys A and B is the Cu content. The alloys were cast, homogenized, and hot and cold rolled to 1.9-mm sheets. The samples were solution treated for 20 minutes at 560 °C in air and quenched in ice water. After quenching, samples were either naturally aged for 30 days or subject to preaging at 100 °C for 50 minutes. After preaging, the samples were stored at room temperature for 30 days prior to artificial aging. Artificial aging was carried out at a temperature of 175 °C to imitate the paint bake temperature used in automotive applications.

Rockwell 15T hardness measurements were carried out in a Wilson hardness tester. Differential scanning calorimetry (DSC) analysis was performed in a PERKIN-ELMER\*

\*PERKIN-ELMER is a trademark of Perkin-Elmer Physical Electronics, Eden Prairie, MN.

DSC-7. During DSC measurements, samples were protected with flowing argon. A high purity Al sample of a similar mass to that of the specimen was used as a reference. Transmission electron microscopy (TEM) was carried out in a PHILIPS\*\* TM420 microscope operating at 120 kV. The

\*\*PHILIPS is a trademark of Philips Electronic Instruments Corp., Mahwah, NJ.

TEM specimens were prepared by jet polishing in 30 vol pct HNO<sub>3</sub>–70 vol pct CH<sub>3</sub>OH solution at –20 °C to –30 °C.

## III. RESULTS

### A. Precipitation Sequence in the As-Quenched Alloys

Figure 1 presents the DSC curves obtained at a heating rate of 10 °C/min for alloys A and B immediately after solutionizing and quenching. For alloy A, the peaks on the DSC curve correspond to the precipitation events as follows.<sup>[23]</sup> Exothermic peak I—GP zone and/or cluster formation; exothermic peak II— $\beta''$  precipitation; exothermic peak III—precipitation of rodlike  $\beta'$  and lathlike precipitates; and exothermic peak IV—formation of  $\beta$  and Si. The broad endothermic peak between peaks I and II corresponds to the dissolution of GP zones, and the endothermic peak V is caused by the dissolution of  $\beta$  and Si.

Figure 2 shows a bright-field TEM micrograph of alloy A heated just over peak III (310 °C) at a heating rate of 10 °C/min. At first sight, rodlike precipitates with different diameters were observed along [010]<sub>Al</sub> and [100]<sub>Al</sub> directions. However, close examination of the end-on section of these precipitates revealed rectangle shape in addition to round shape. The round-shape precipitates are  $\beta'$  viewed end-on.<sup>[8]</sup> The rectangle-shape cross sections of some of the precipitates suggest that the corresponding precipitates are lathlike. The appearance of lathlike precipitates has been

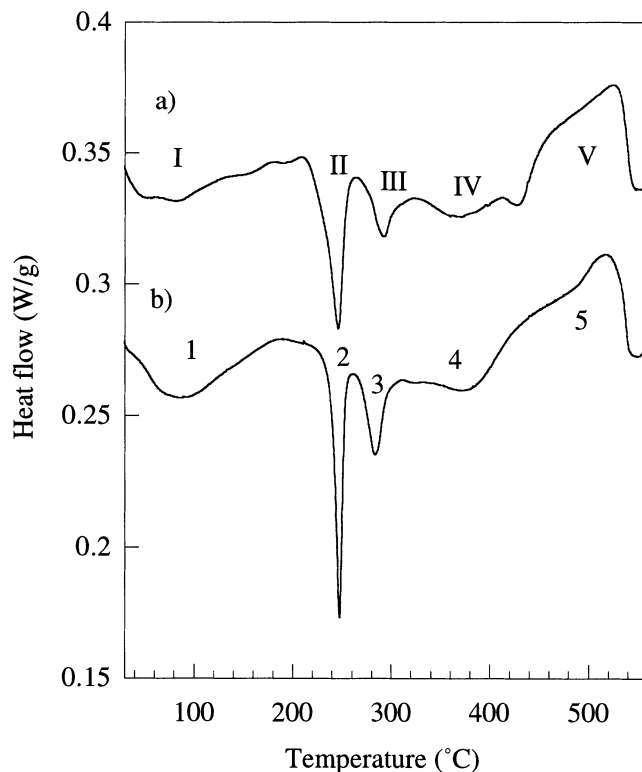


Fig. 1—DSC traces, taken at a scan rate of 10 °C/min, of samples immediately after solutionizing and quenching: (a) alloy A and (b) alloy B.

previously reported in Al-Mg-Si(-Cu) alloys.<sup>[4,15,24]</sup> Chakrabarti *et al.*<sup>[15]</sup> believe that the lath-shaped phase is a precursor of the  $Q$  phase and have suggested that this phase be denoted as  $Q'$ .

In Figure 3, the schematic diffraction pattern, simulated from published data,<sup>[8,24]</sup> of a  $\beta'$  variant and a  $Q'$  variant is compared with the enlarged diffraction pattern in Figure 2. It is clearly seen that (0221) $_{\beta'}$  and (2131) $_{Q'}$  match the two maxima on the streak in the diffraction pattern (Figure 3(b)) very well. In addition, faint rings can be seen in the diffraction pattern, and the positions of the rings are very close to those reported in Reference 15. These rings are from  $Q'$  precipitates whose  $c$ -axes are parallel to [001]<sub>Al</sub>.<sup>[15]</sup> Therefore, it is believed that the precipitation event corresponding to peak III on the DSC trace for alloy A is the simultaneous precipitation of  $\beta'$  and  $Q'$ .

To reveal to which precipitation reactions the peaks on the DSC curve of alloy B (Figure 1b) correspond, TEM observations were made on samples annealed in the DSC at a heating rate of 10 °C/min to temperatures just above the end of the corresponding peaks. For the sample heated just over the DSC peak 1, no ordered precipitates were observed by TEM. However, comparison with previous results suggests that DSC peak 1 is associated with the formation of GP zones.<sup>[1,3,4]</sup>

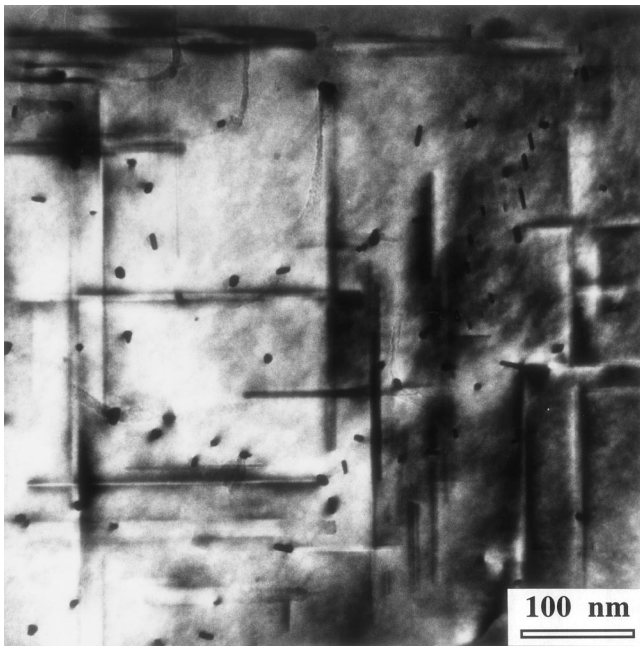


Fig. 2—Bright-field TEM micrograph of alloy A heated to just over DSC peak II shown in Fig. 1(a), revealing the rectangle and round shapes when the precipitates are viewed end-on.

Figure 4 shows a bright-field TEM micrograph and the corresponding  $[001]_{Al}$  selected area diffraction pattern of alloy B heated at  $10\text{ }^{\circ}\text{C}/\text{min}$  to  $260\text{ }^{\circ}\text{C}$  (just over peak 2). The bright-field image revealed a strain contrast of needlelike precipitates oriented along  $[010]_{Al}$  and  $[100]_{Al}$  directions together with some fine dots. The needles were typically 20- to 40-nm long. Most of the dots should be the end-on sections of the needles along  $[001]_{Al}$ . The dark-field image showed that the diameter of the needles was in the range of 2 to 5 nm. The selected area diffraction pattern showed faint streaks along  $[010]_{Al}$  and  $[100]_{Al}$  due to the needlelike precipitates.<sup>[1,4]</sup> This indicates that DSC peak 2 corresponds to the precipitation of  $\beta'$ .

Figure 5 shows a bright-field TEM micrograph and the corresponding  $[001]_{Al}$  selected area diffraction pattern of alloy B heated just over DSC peak 3 in Figure 1(b) at a heating rate of  $10\text{ }^{\circ}\text{C}/\text{min}$ . Although it seemed that rodlike or needlelike precipitates with different diameters were observed along  $[010]_{Al}$  and  $[100]_{Al}$  directions, close examination of the end-on section of these precipitates revealed that most of them were rectangle shape. This suggests that the corresponding precipitates are lathlike. In addition, for most of the lathlike precipitates, both the width direction and the axial direction appeared to be parallel to the  $\langle 100 \rangle_{Al}$  directions. This corresponds to a habit plane of  $\{100\}_{Al}$ . The diffraction pattern contained streaks with intensity maxima at  $\{21\bar{3}1\}_{Q'}$  and some faint rings. The distinct lath-shape appearance of the precipitates and the characteristics of the diffraction pattern suggest that DSC peak 3 in Figure 1(b) should correspond to the precipitation of  $Q'$  phase.<sup>[15]</sup>

The microstructure of alloy B heated to  $400\text{ }^{\circ}\text{C}$  (end of DSC peak 4 in Figure 1(b)) was also examined. Both bright-field and dark-field observations show large particles and lathlike precipitates (the end-on view is rectangle), as shown in Figure 6. Close examination of the dark-field image

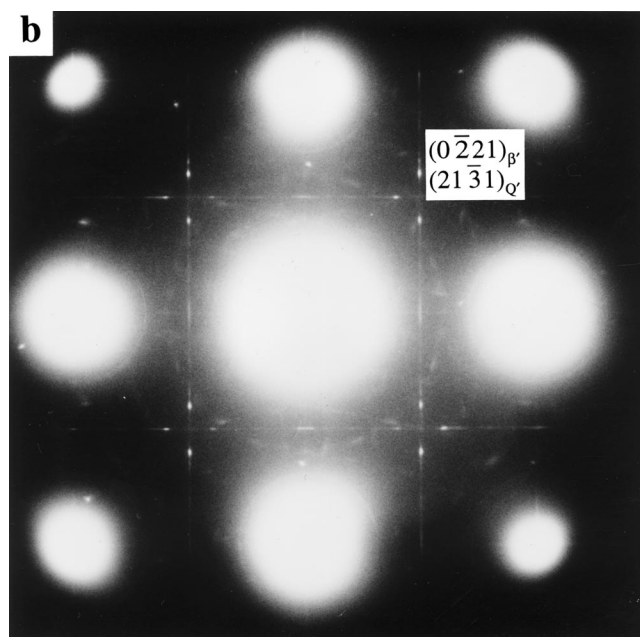
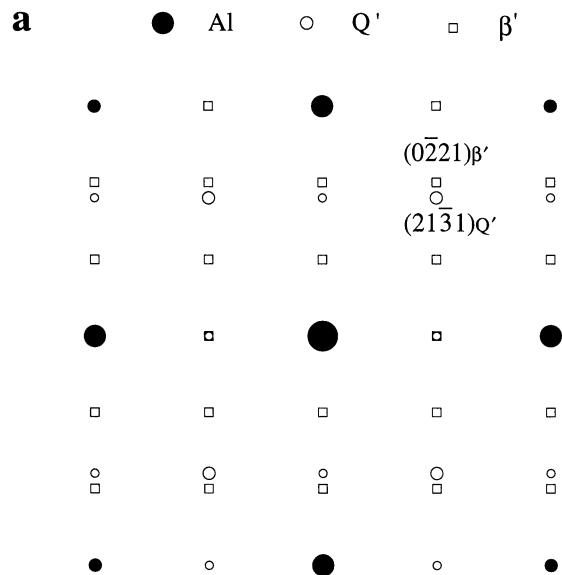


Fig. 3—(a) A simulated diffraction pattern of  $\beta'$  and  $Q'$  in Al matrix with the orientation relationships of  $[100]_{Al}/[0001]_{\beta'}$ ,  $(020)_{Al}/(0220)_{\beta'}$  and  $[100]_{Al}/[0001]_{Q'}$ ,  $(020)_{Al}/(2130)_{Q'}$ , and (b) the selected area diffraction pattern ( $[001]$  zone axis) corresponding to Fig. 2. Notice the good match of  $(0221)_{\beta'}$ , and  $(21\bar{3}1)_{Q'}$ , on the two diffraction patterns.

reveals that, at this stage, the laths no longer lie on  $\{100\}_{Al}$  planes. While the axial direction is still parallel to  $\langle 100 \rangle_{Al}$ , the width direction and thickness direction are off  $\langle 100 \rangle_{Al}$  by 10 to 12 deg, indicating a habit plane close to  $\{015\}_{Al}$ .<sup>[24]</sup> The streaks in the diffraction pattern, the positions of the intensity maxima, and the lathlike morphology are the characteristics of  $Q$  phase.<sup>[15]</sup> Microdiffraction analysis showed that the large particles were Si. This suggests that the DSC peak 4 in Figure 1(b) corresponds to the precipitation of  $Q$  and Si. The broad endothermic peak (peak 5) on the DSC curve in Figure 1(b) is caused by the dissolution of these precipitates.

Based on the aforementioned DSC measurements and

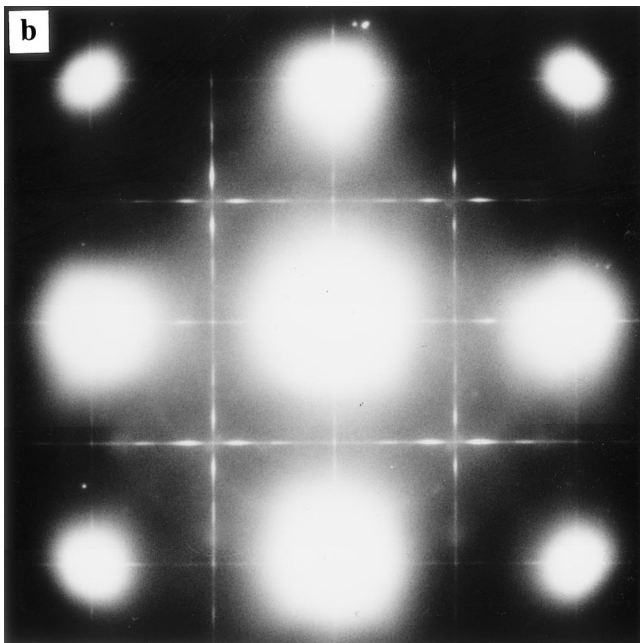
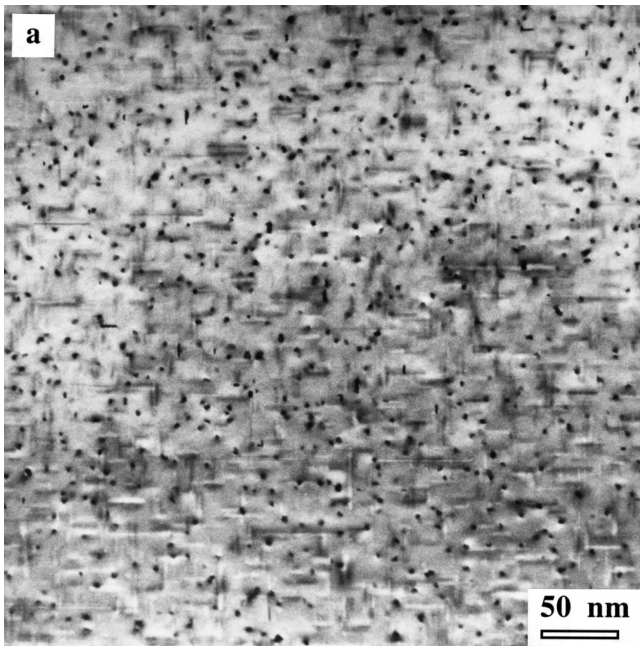


Fig. 4—(a) Bright-field TEM micrograph and (b) the corresponding  $[001]_{\text{Al}}$  diffraction pattern of alloy B heated at a heating rate of  $10\text{ }^{\circ}\text{C}/\text{min}$  to the end of DSC peak 2 shown in Fig. 1(b). The needlelike morphology and the  $\langle 100 \rangle_{\text{Al}}$  streaks in the diffraction pattern suggest that the precipitates are  $\beta''$ .

TEM observations, the precipitation sequence in alloy A is believed to be as follows: GP zones  $\rightarrow$  needlelike  $\beta'' \rightarrow$  rodlike  $\beta' +$  lathlike  $Q' \rightarrow \beta + \text{Si}$ . On the other hand, the precipitation sequence in alloy B is GP zones  $\rightarrow$  needlelike  $\beta'' \rightarrow$  lathlike  $Q' \rightarrow$  lathlike  $Q + \text{Si}$ .

#### B. Phase Equilibria of 6022 Type Alloys

Since the major compositional difference between alloys A and B is the Cu content, a pseudobinary phase diagram

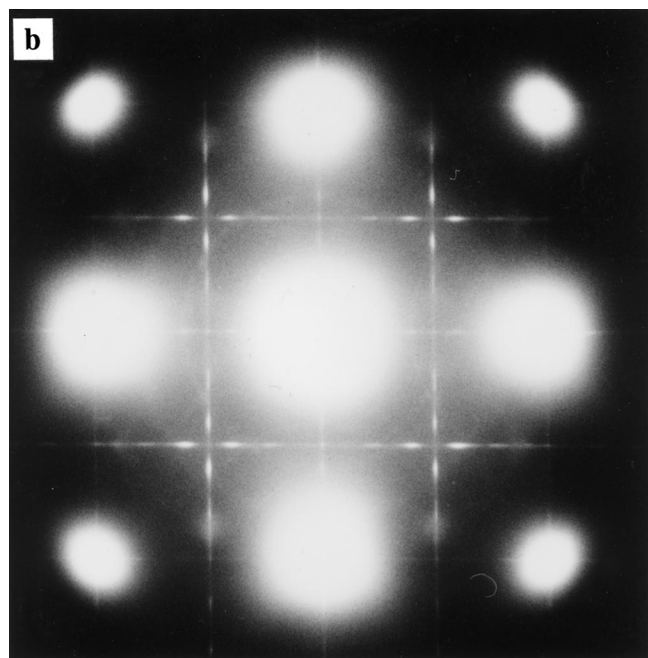
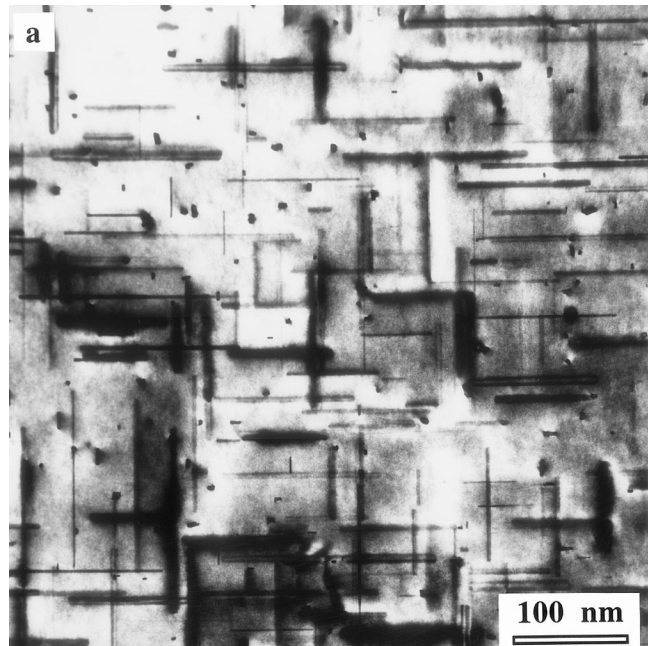


Fig. 5—(a) Lath-shaped precipitates corresponding to DSC peak 3 in Fig. 1(b).  $[001]_{\text{Al}}$  selected area diffraction pattern.

of (Al-0.55 wt pct Mg-1.28 wt pct Si)-Cu would be very helpful to the understanding of precipitation sequence in these 6022 type alloys. Figure 7 presents part of the (Al-0.55 wt pct Mg-1.28 wt pct Si)-Cu phase diagram, calculated by a software called ThermoCalc.<sup>[25]</sup> It is seen that for alloy A (0.07 wt pct Cu), the equilibrium precipitates are  $\beta$  ( $\text{Mg}_2\text{Si}$ ),  $Q$  ( $\text{Al}_5\text{Cu}_2\text{Mg}_8\text{Si}_6$ ), and Si under  $\sim 300\text{ }^{\circ}\text{C}$ . Between  $\sim 300\text{ }^{\circ}\text{C}$  and  $\sim 540\text{ }^{\circ}\text{C}$ ,  $\beta$  and Si become the equilibrium precipitates. For alloy B (0.91 wt pct Cu), on the other hand,  $\theta$ ,  $Q$ , and Si are the equilibrium precipitates below  $\sim 320\text{ }^{\circ}\text{C}$ . Between  $\sim 320\text{ }^{\circ}\text{C}$  and  $\sim 460\text{ }^{\circ}\text{C}$ ,  $Q$  and Si remain as the equilibrium precipitates. Interestingly,  $\beta$  becomes one of the equilibrium precipitates between  $\sim 460\text{ }^{\circ}\text{C}$  and  $\sim 530\text{ }^{\circ}\text{C}$ .

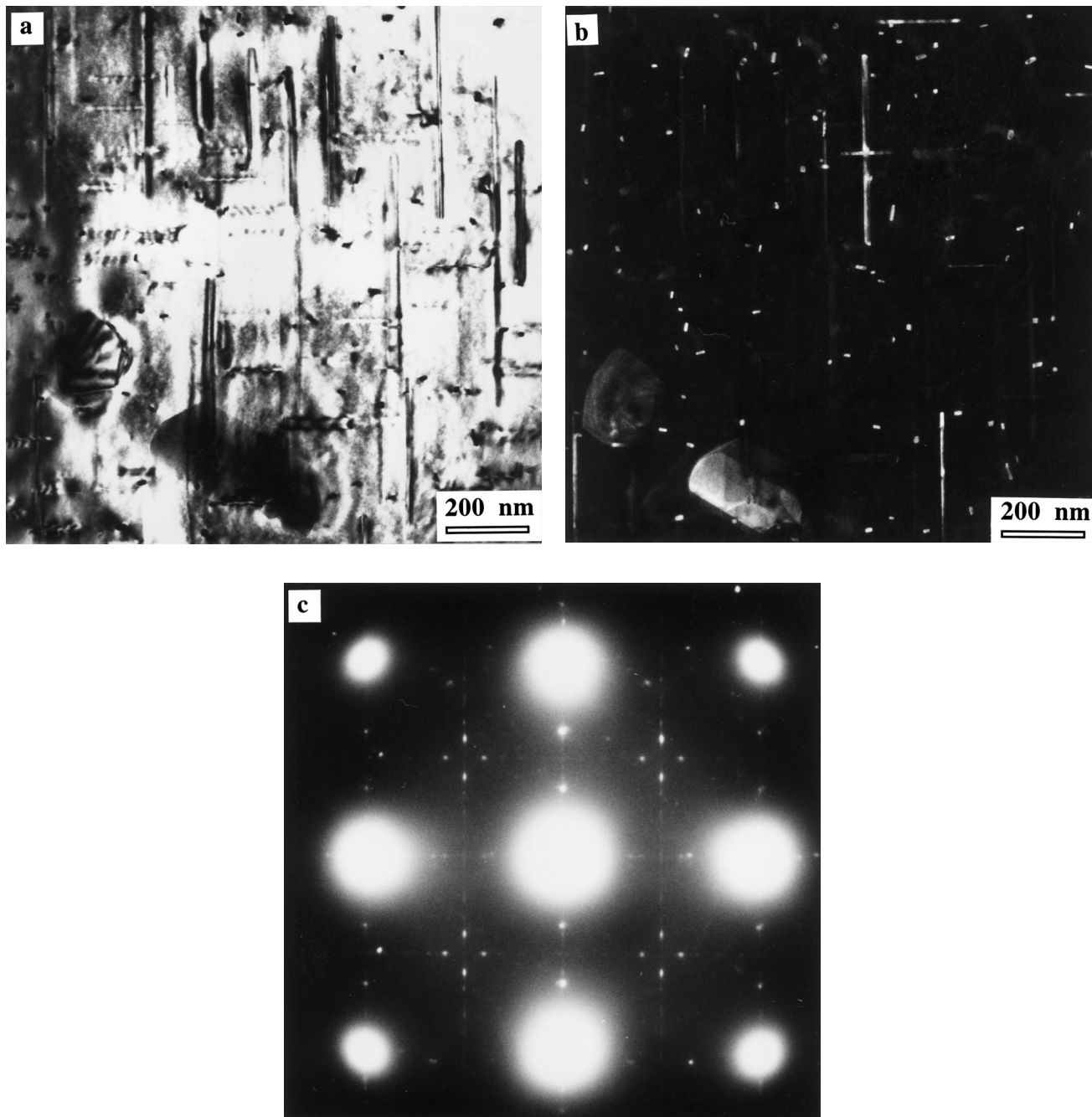


Fig. 6—(a) Bright-field and (b) dark-field TEM images of alloy B heated to the end of DSC peak 4 in Fig. 1(b). Two kinds of precipitates, *i.e.*, lath-shaped precipitates and large particles, are observed. (c) Corresponding  $[001]_{Al}$  selected area diffraction pattern.

Figure 8 shows the variation of mole fraction of the equilibrium precipitates with temperature, calculated by ThermoCalc, for alloy A. It is seen that Si,  $\beta$ , and  $Q$  coexist below  $\sim 320$  °C. However, the mole fraction of  $Q$  decreases with increasing temperature and disappears above  $\sim 320$  °C. The mole fractions of Si and  $\beta$  also decrease with increasing temperature at higher temperatures. At around 550 °C, both of them dissolve into the matrix.

Figure 9 shows the variation of mole fraction of the equilibrium precipitates with temperature, calculated by ThermoCalc, for alloy B. It is seen that  $Q$  predominates at lower temperatures. Silicon and  $\theta$  are also present as equilibrium

precipitates. However,  $\theta$  disappears above  $\sim 320$  °C. At higher temperatures, while the mole fractions of  $Q$  and Si decrease with increasing temperature,  $\beta$  begins to become an equilibrium precipitate from  $\sim 480$  °C until it dissolves at around 540 °C. Both  $Q$  and Si dissolve into the matrix at 520 °C and 550 °C, respectively.

### C. Effect of Natural Aging and PreAging on the Precipitation Characteristics

Figure 10 displays the DSC traces of alloys A and B naturally aged for 30 days after solutionizing and quenching.

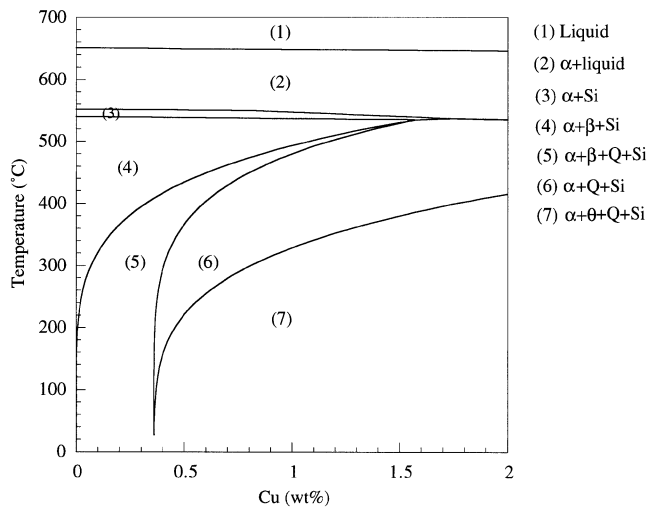


Fig. 7—A section of pseudo-binary phase diagram for (Al-0.55 wt pct Mg-1.28 wt pct Si)-Cu.

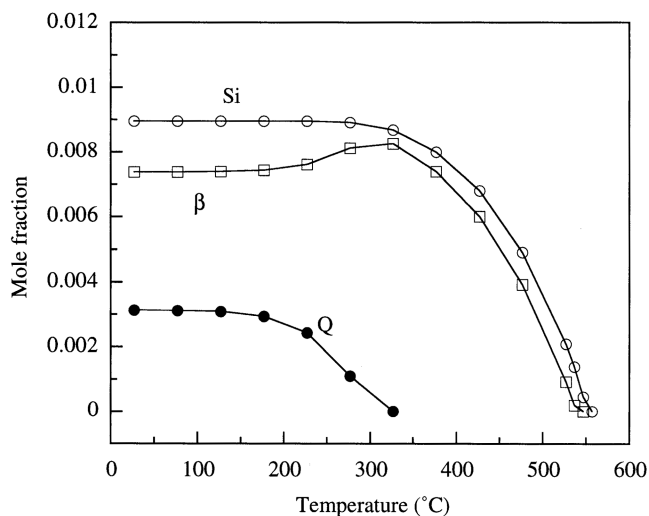


Fig. 8—Variation of mole fractions of the equilibrium precipitates with temperature for alloy A.

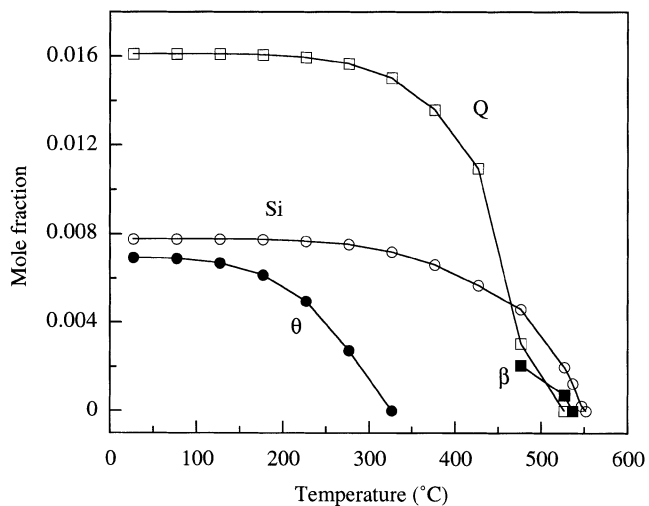


Fig. 9—Dependence of mole fractions of the equilibrium precipitates on temperature for alloy B.

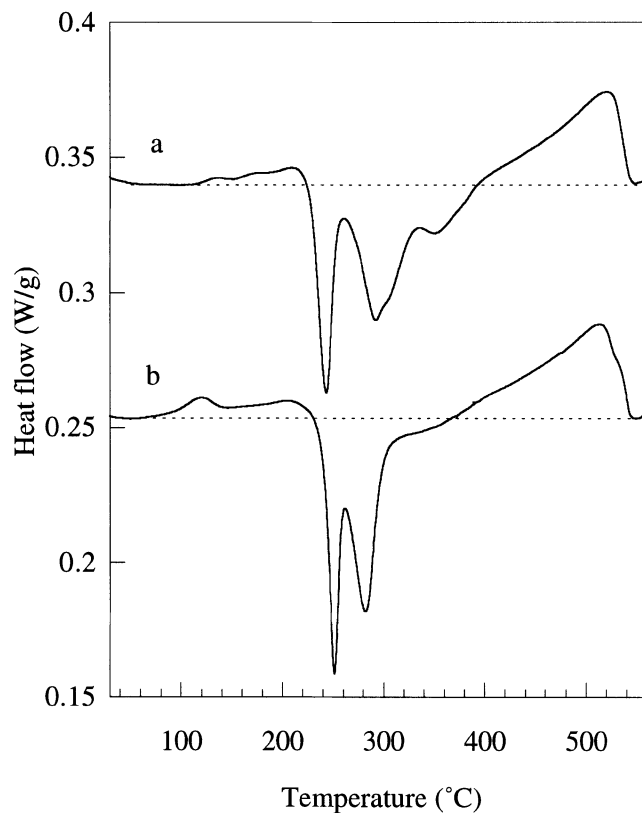


Fig. 10—DSC curves (scan rate 10 °C/min) of (a) alloy A naturally aged for 30 days and (b) alloy B naturally aged for 30 days.

For both alloys A and B, compared with the DSC curves of as-quenched samples (Figure 1), the main difference is the disappearance of the peaks corresponding to GP zone formation. This indicates that GP zones already formed during natural aging. The broad endothermic peaks (110 °C to 215 °C for alloy A and 80 °C to 225 °C for alloy B, respectively) are thought to be caused by the dissolution of the GP zones in the naturally aged samples.<sup>[19,26]</sup> The DSC peaks at higher temperatures were similar to those of the as-quenched alloy (Figure 1 (a)) and should correspond to the same precipitation events.

Figure 11 shows the DSC traces of alloys A and B preaged at 100 °C for 50 minutes followed by 30 days of natural aging. It is seen that for both alloys A and B, the broad exothermic peaks centered at around 90 °C on the DSC curves of the as-quenched samples did not appear on the DSC curves of the preaged samples either. On the other hand, the DSC peak corresponding to  $\beta''$  precipitation did appear on each of the DSC curves, indicating that the precipitates formed during preaging and the following natural aging were GP zones. Some of the GP zones may have been dissolved before the precipitation of  $\beta''$ , as suggested by the small endothermic bumps between 150 °C and 210 °C on the DSC curves. The additional small exothermic peaks, such as the one at around 245 °C, suggest that there might be some metastable precipitates in addition to the normal precipitation events, as described in section III-A.<sup>[19]</sup>

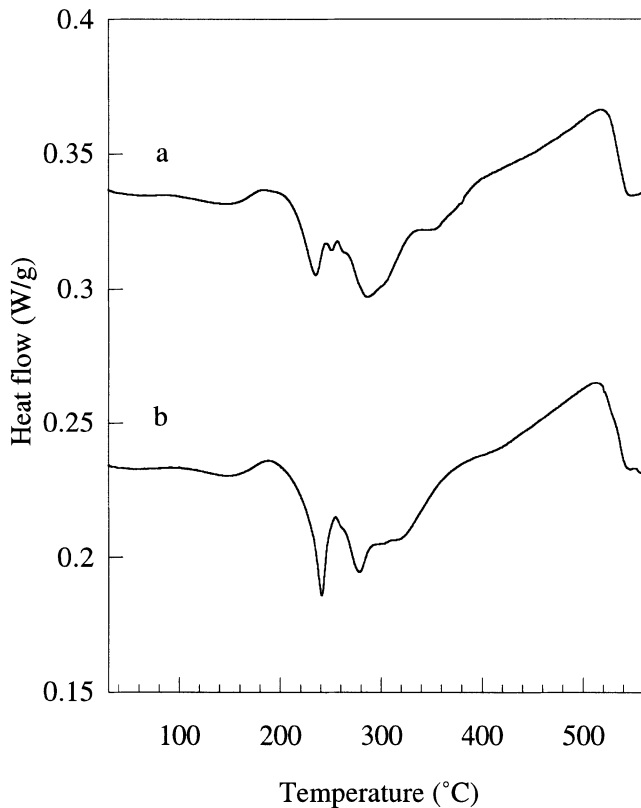


Fig. 11—DSC traces (scan rate 10 °C/min) of alloys preaged at 100 °C for 50 min followed by 30 days of natural aging: (a) alloy A and (b) alloy B.

#### D. Precipitation Hardening Behavior

##### 1. Artificial aging response

Artificial age hardening curves at a temperature of 175 °C for as-quenched alloys A and B are shown in Figure 12. For both alloys A and B, the hardness increased with increasing artificial aging time and reached the peak at around 500 minutes. In addition, alloy B (with higher Cu content) showed faster age hardening kinetics. It is clear that for the simulated paint bake condition (20 minutes at 175 °C; arrow, Figure 12), both alloys are still in an under-aged condition.

Figure 13 presents the effect of 30 days natural aging on the artificial aging response at 175 °C for alloys A and B. As expected, the naturally aged samples exhibited higher initial hardness when compared with samples that had not been naturally aged. However, for artificial aging times up to 200 minutes, the hardnesses of the naturally aged alloys were lower than those of the as-quenched counterparts. In addition, the naturally aged samples showed decreases in hardness upon initial artificial aging, *i.e.*, artificial aging at 175 °C for short times (*e.g.*, 20 minutes; arrow, Figure 13) actually softened the alloys. Nevertheless, after artificial aging, the hardness of alloy B was greater than that of alloy A.

The artificial aging response at 175 °C for different times of the samples preaged at 100 °C for 50 minutes and then naturally aged for 30 days is shown in Figure 14. Unlike the samples only naturally aged for 30 days, samples preaged at 100 °C for 50 minutes and then naturally aged for 30 days did not show any decrease in the initial artificial aging stage. As the artificial aging time increased, the hardness

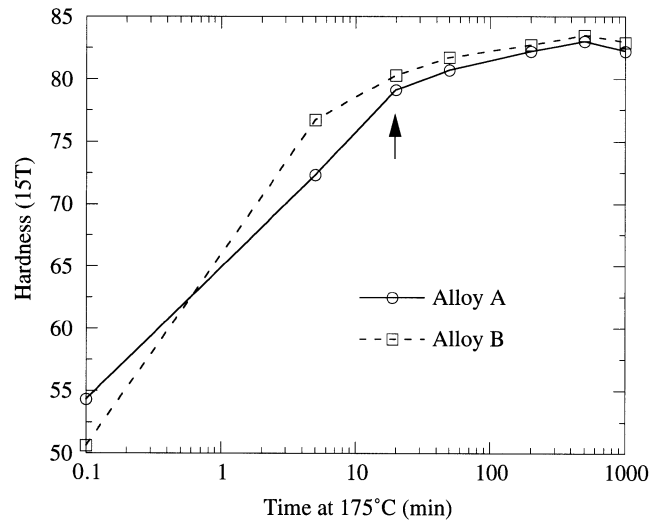


Fig. 12—Variation of hardness with the artificial aging time at 175 °C for as-quenched alloys.

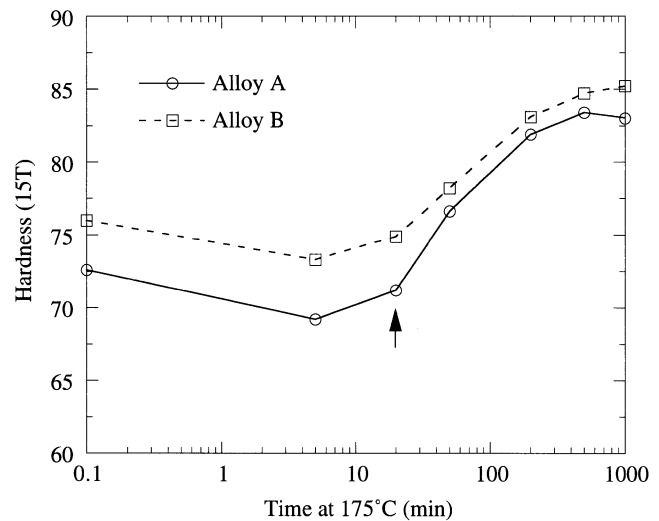


Fig. 13—Dependence of hardness on the artificial aging time at 175 °C for alloys naturally aged for 30 days.

increased until peak values were reached. It is seen that after artificial aging, the values of the peak hardness for the preaged samples were more or less the same as those of the naturally aged samples. For the simulated paint bake condition (20 minutes at 175 °C; arrow, Figure 14), however, the values of the hardness of the preaged samples were considerably higher than those of the naturally aged counterparts. This indicates that suitable preaging is able to significantly reduce the detrimental effect of natural aging on the artificial aging kinetics.

##### 2. Microstructural observations

The microstructural changes during the age hardening process in alloys A and B were monitored by transmission electron microscopy. It should be mentioned that for naturally aged or preaged samples, no evidence of clusters or GP zones could be observed from either bright-field images or selected area electron diffraction patterns. However, based on the aforementioned DSC results and previous studies,<sup>[4,26]</sup>

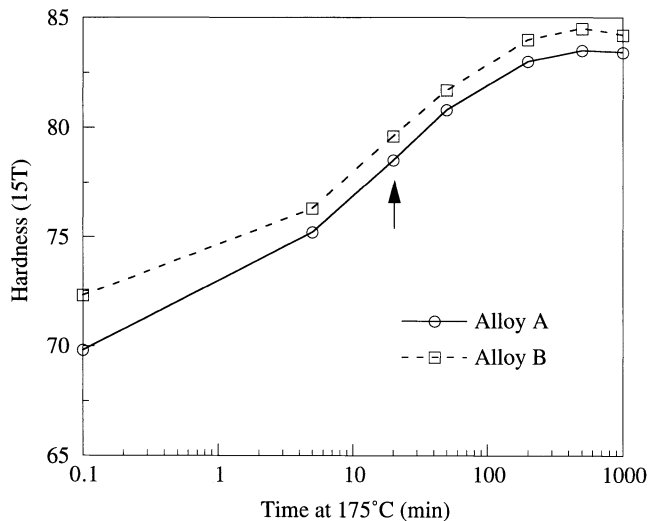


Fig. 14—Dependence of hardness on the artificial aging time at 175 °C for alloys preaged at 100 °C for 50 min followed by 30 days of natural aging.

ultrafine GP zones or clusters should exist in both naturally aged and preaged samples.

Figure 15 shows the microstructure of alloys A and B artificially aged at 175 °C for 20 minutes after natural aging for 30 days. No distinct features of precipitates were observed for either alloy A or B. The corresponding diffraction patterns did not show any streaks either. The weak spots in the diffraction patterns could be due to oxidation or contamination during and/or after jet polishing.<sup>[4]</sup>

Figure 16 displays bright-field TEM micrographs and the corresponding selected area diffraction patterns of alloys A and B artificially aged at 175 °C for 20 minutes after being preaged at 100 °C for 50 minutes and naturally aged for 30 days. The bright-field micrographs show only dotlike precipitates to be present for both alloys. However, the diffraction patterns revealed streaks along  $[100]_{Al}$  and  $[010]_{Al}$  directions. The streaks were caused by needle precipitates along  $\langle 001 \rangle_{Al}$  orientations.<sup>[27]</sup> Most of the dotlike precipitates are needles viewed end-on. Needles along  $[100]_{Al}$  and  $[010]_{Al}$  directions were not clearly visible, largely due to very small strain contrast since these needle precipitates are coherent with the matrix.<sup>[28]</sup>

Figure 17 shows TEM micrographs of alloys A and B artificially aged at 175 °C for 1000 minutes after natural aging for 30 days. At this stage, in alloy A, the length of the needles increased to  $\sim 50$  nm and the diameter increased to  $\sim 5$  nm. On the other hand, in addition to the aforementioned needles, thinner ( $\sim 3$  nm in diameter) but longer ( $\sim 150$  nm in length) needles were also observed in alloy B. Figure 18 shows bright-field images of alloys A and B artificially aged at 175 °C for 1000 minutes after preaging at 100 °C for 50 minutes followed by 30 days natural aging. It is seen for either alloy A or B, after artificial aging at 175 °C for 1000 minutes, that the microstructure of the preaged sample was very similar to that of the naturally aged sample. This is in agreement with the results of the hardness measurements, which show that the values of peak hardness were more or less the same regardless of preaging conditions.

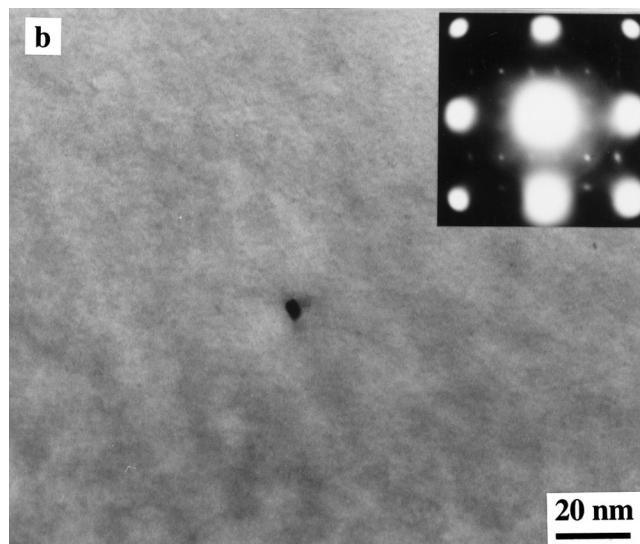
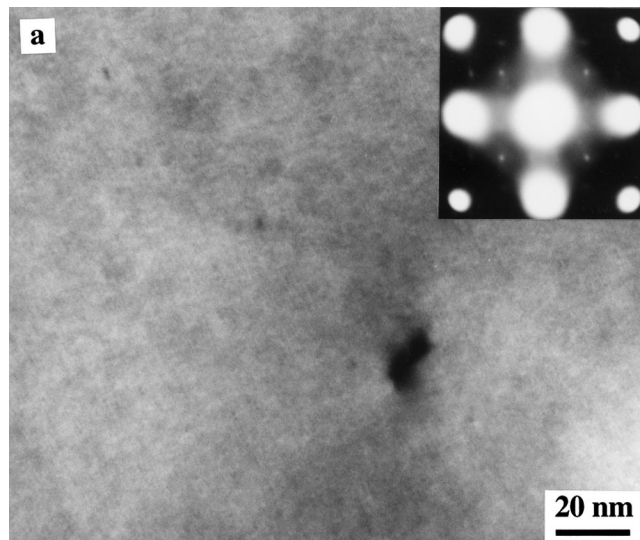


Fig. 15—Bright-field TEM micrographs and the corresponding selected area electron diffraction patterns of samples artificially aged at 175 °C for 20 min after natural aging for 30 days: (a) alloy A and (b) alloy B.

## IV. DISCUSSION

### A. Effect of Cu Content on the Precipitation Sequence and Age Hardening Behavior

The first stage in the precipitation sequence, *i.e.*, GP zone or cluster formation, is a complex process. Based on previous studies, this stage could consist of three types of clusters: clusters of Si atoms, clusters of Mg atoms, and coclusters of Mg and Si atoms.<sup>[4]</sup> These three types of clusters compete with each other. However, due to the ultrafine scale of the clusters, the details of the clustering process are by no means clear. According to a recent three-dimensional atom probe study, at this stage, Cu did not have a significant effect on the chemical composition of the GP zones.<sup>[29]</sup>

Previous investigations show that  $\beta''$  is the dominant intermediate phase present in both Al-Mg-Si and Al-Mg-Si-Cu alloys in the second stage of the precipitation sequence.<sup>[4,15]</sup> The  $\beta''$  phase is needle shaped with the axial direction along  $\langle 100 \rangle_{Al}$  and is based on the monoclinic crystal system.<sup>[4-7]</sup>

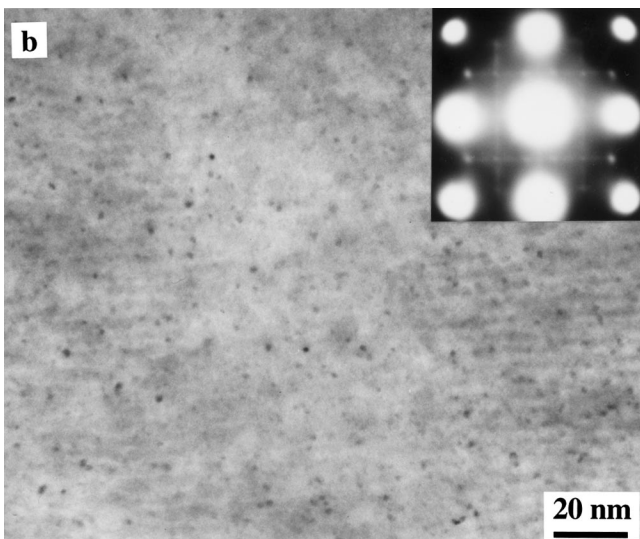
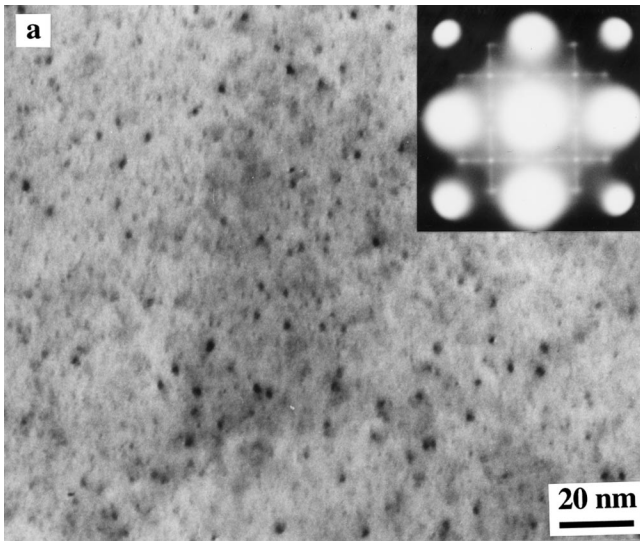


Fig. 16—Microstructures of samples artificially aged at 175 °C for 20 min after preaging at 100 °C for 50 min followed by 30 days of natural aging: (a) alloy A and (b) alloy B.

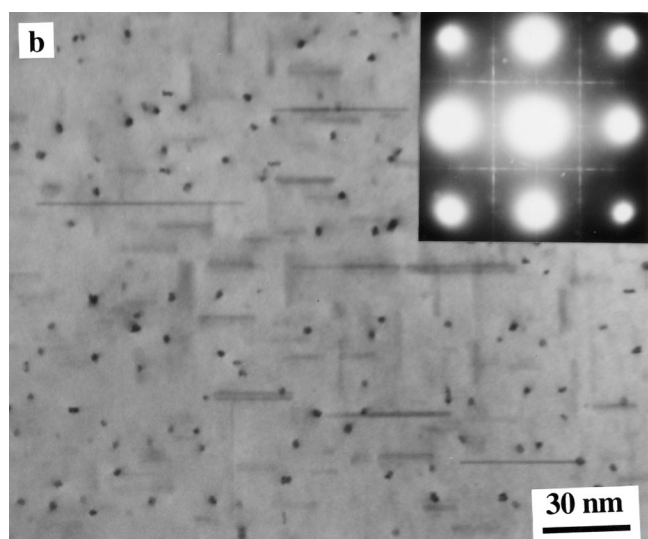
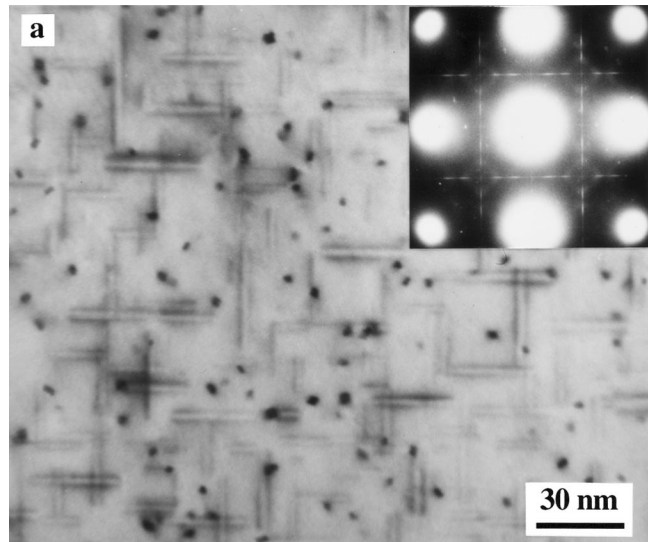


Fig. 17—Bright-field TEM micrographs and the corresponding selected area electron diffraction patterns of samples artificially aged at 175 °C for 1000 min after natural aging for 30 days: (a) alloy A and (b) alloy B.

However, the Cu content and Mg:Si ratio could influence the lattice parameters of the  $\beta''$  phase.<sup>[4–7]</sup> For the high Cu alloy, Cu atoms were found to be incorporated into the needlelike  $\beta''$  precipitates,<sup>[29]</sup> suggesting that the needlelike precipitates may be a precursor to the metastable phase of  $Q$ .

Copper has a significant effect on the third stage of the precipitation sequence. For Al-Mg-Si alloys, the third stage in the precipitation sequence is rod-shaped  $\beta'$  phase aligned along  $\langle 100 \rangle_{\text{Al}}$ .<sup>[8,28]</sup> The structure of the  $\beta'$  phase is hexagonal with  $a = 0.705$  nm and  $c = 0.405$  nm.<sup>[8]</sup> On the other hand, with the addition of Cu to Al-Mg-Si alloys, lath-shaped precipitates would appear. The lath-shaped phase was originally observed in a 6061 alloy by Dumult *et al.*, who thought it was a modified  $\beta'$  and called it  $B'$ .<sup>[24]</sup> Later investigations<sup>[30,31]</sup> have confirmed the distinct lath precipitate morphology in Al-Mg-Si-Cu alloys. In addition, the amount of the lath-shaped precipitate would increase with increased Cu content.<sup>[31]</sup> More recently, Chakrabarti *et al.* have suggested that the lath-shaped phase is a precursor of the  $Q$

phase and called it  $Q'$ .<sup>[15]</sup> It is interesting to note that in this study, lath-shaped  $Q'$  also appeared at the third stage of precipitation sequence in alloy A, which only contained 0.07 wt pct Cu. The reason for this is that the formation of  $Q'$  is kinetically favored compared with competing phases.<sup>[15]</sup> It is also noted that both  $Q$  and  $\beta$  are equilibrium precipitates for temperatures below 300 °C (Figure 8), so the coexistence of  $Q'$  and  $\beta'$  should not be surprising.

The role of Cu in the precipitation hardening of Al-Mg-Si alloys has been investigated previously by a number of authors.<sup>[20,32,33]</sup> Pashley *et al.*<sup>[20]</sup> reported that the presence of Cu led to a much finer precipitate structure in the artificially aged samples, and thus gave rise to better strength after artificial aging. Similar results were also reported by Suzuki *et al.*<sup>[32]</sup> The addition of Cu was also reported to alleviate the deleterious effects of natural aging.<sup>[20,33]</sup> In the present study, it seemed that Cu had a small effect on the peak hardness developed during aging at 175 °C. However, under the artificial aging condition of 175 °C  $\times$  20 min,

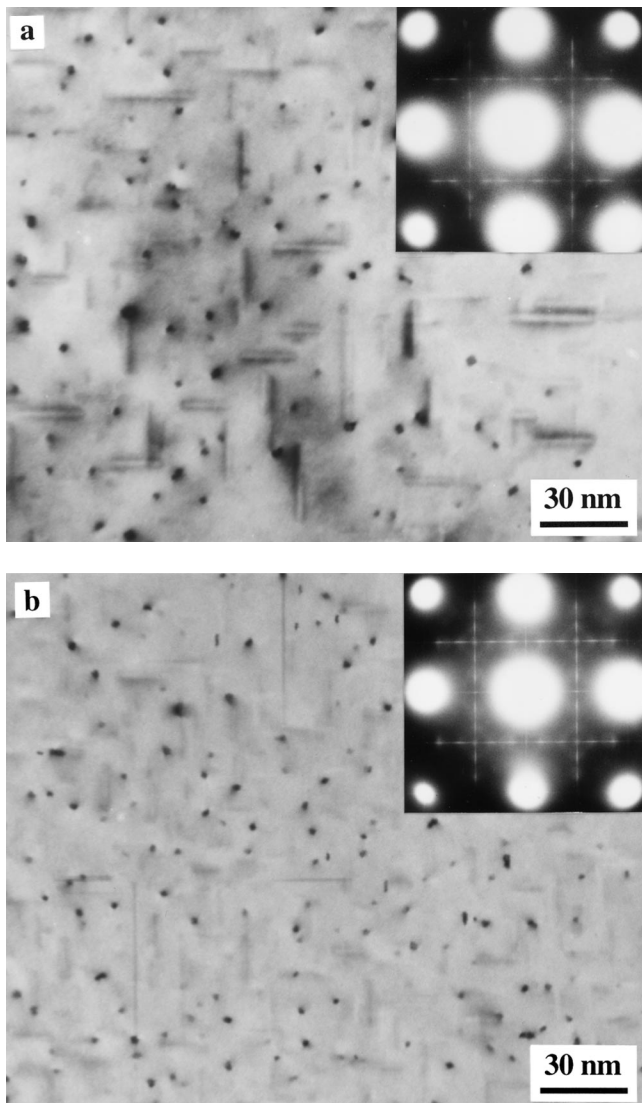


Fig. 18—Bright-field TEM micrographs and the corresponding selected area electron diffraction patterns of samples artificially aged at 175 °C for 1000 min after preaging at 100 °C for 50 min followed by 30 days of natural aging: (a) alloy A and (b) alloy B.

regardless of the preaging condition, Cu enhanced the artificial aging response. This could be related to the precipitation of precursor metastable phases of  $Q$  in the higher Cu alloy.<sup>[15]</sup> However, further work is needed to clarify the mechanism.

#### B. Effect of Preaging on the Artificial Age Hardening Behavior

Although preaging has been shown to significantly affect the age hardening characteristics in Al-Mg-Si-(Cu) alloys, the mechanisms of the effects are still not completely understood. It appears that a critical preaging temperature exists for a specific alloy. If the alloy is preaged below that temperature, preaging usually shows a negative effect on artificial aging. Natural aging is such a case.<sup>[20,21]</sup> From DSC,<sup>[23]</sup> hardness and electrical-resistivity measurements,<sup>[20]</sup> it is inferred that zones must have formed during natural aging. It has been previously suggested that these zones could act as nuclei for precipitates formed during artificial aging.<sup>[20]</sup>

In a recent study of the effect of preaging on precipitation hardening behavior in an Al-Mg-Si alloy, Saga *et al.*<sup>[34]</sup> speculated that GP-I zones formed when the alloy is preaged below  $\sim 67$  °C. These zones coexist with GP-II zones ( $\beta''$ ) formed during subsequent artificial aging and hence produce a coarser precipitate microstructure. On the other hand, when the alloy is preaged above  $\sim 67$  °C, Saga *et al.* suggested that fine  $\beta''$  formed directly during preaging treatment.

The present DSC and hardness measurements suggest that GP zones formed during natural aging are not stable. For naturally aged samples, artificial aging at 175 °C for 20 minutes did not harden the materials or produce any recognizable precipitates. This indicates that a reversion of the zones formed during natural aging must have taken place during artificial aging. In other words, GP zones formed during natural aging are unlikely to act as nuclei during artificial aging. Furthermore, even for samples preaged at 100 °C for 50 minutes, there is no TEM evidence about the formation of  $\beta''$ . The lower hardnesses of preaged samples than those of the naturally aged counterparts also suggest that the direct formation of  $\beta''$  seems unlikely.

A possible explanation of the preaging effect is that preaging parameters affect the distribution and size of the clusters formed during preaging. Dependent on the critical stable nuclei size, the clusters could either dissolve or act as nucleation sites during subsequent artificial aging. On the assumption that the rate of clustering at any temperature below 100 °C is governed by the concentration of quenched-in vacancies, it has been proposed that if there is no interaction between vacancies and GP zones formed during preaging, the vacancies can accompany the solute atoms to the zones and hence return to the matrix.<sup>[35]</sup> Natural aging of 6022 type alloys may fall into this category. During natural aging, with the formation of clusters or GP zones, the hardnesses increase with increasing time. As vacancies move to the GP zones with solute atoms, the materials harden further. However, as time increases, the vacancy concentrations in the zones and the matrix will reach their equilibrium values. As a result, the hardness will reach a plateau.<sup>[26]</sup> During subsequent artificial aging, GP zones will no longer sustain higher vacancy concentration than that in the matrix; thus, some vacancies and solute atoms in the GP zones will go back to the matrix and cause the materials to soften slightly during initial artificial aging. If, on the other hand, a substantial energy of binding exists between vacancies and GP zones, as the vacancies arrive at the GP zones, they will be “locked” there.<sup>[35]</sup> In this case, the GP zones are expected to act as nuclei for the precipitation of  $\beta''$ . This may explain why for 6022-type alloys, preaging at 100 °C enhanced the artificial aging responses in the initial stage.

## V. CONCLUSIONS

In a typical 6022 alloy, which contains a small amount of Cu, the precipitation sequence consists of  $\alpha$  (sss)  $\rightarrow$  GP zones  $\rightarrow$  needlelike  $\beta''$   $\rightarrow$  rodlike  $\beta'$  + lath-shaped  $Q'$   $\rightarrow$   $\beta$  + Si. On the other hand, with the increase of Cu content to 0.91 wt pct, the precipitation sequence becomes  $\alpha$  (sss)  $\rightarrow$  GP zones  $\rightarrow$  needlelike  $\beta''$   $\rightarrow$  lath-shaped  $Q'$   $\rightarrow$   $Q$  + Si.

Preaging has been shown to significantly improve the artificial aging response of 6022 type aluminum alloys in the simulated paint bake condition (20 minutes at 175 °C). It is speculated that the GP zones formed during preaging

exceed the critical stable size and thus can act as nuclei for the precipitation of  $\beta''$  during subsequent artificial aging. On the other hand, naturally aged samples soften after artificial aging in the simulated paint bake condition, indicating that the GP zones formed during natural aging partially dissolved during artificial aging. In any case, a higher Cu level always results in higher hardnesses.

## ACKNOWLEDGMENTS

WFM was partially supported by a grant from the Ford Motor Company. DEL acknowledges a grant from NEDO. The alloys used in this study were provided by ALCOA.

## REFERENCES

- I. Dutta and S.M. Allen: *J. Mater. Sci. Lett.*, 1991, vol. 10, pp. 323-26.
- G.B. Burger, A.K. Gupta, P.W. Jeffrey, and D.J. Lloyd: *Mater. Characterization*, 1995, vol. 35, pp. 23-39.
- L. Zhen, W.D. Fei, S.B. Kang, and H.W. Kim: *J. Mater. Sci.*, 1997, vol. 32, pp. 1895-1902.
- G.A. Edwards, K. Stiller, G.L. Dunlop, and M.J. Couper: *Acta Mater.*, 1998, vol. 46, pp. 3893-1904.
- R.P. Wahi and M. von Heimendahl: *Phys. Status Solidi (a)*, 1974, vol. 24, pp. 607-12.
- J.P. Lynch, L.M. Brown, and M.H. Jacobs: *Acta Metall.*, 1982, vol. 30, pp. 1389-95.
- S.J. Andersen, H.W. Zandbergen, J. Jansen, C. Treholt, U. Tundal, and O. Reiso: *Acta Mater.*, 1998, vol. 46, pp. 3283-98.
- M.H. Jacobs: *Phil. Mag.*, 1972, vol. 26, pp. 1-13.
- K. Matsuda, S. Tada, S. Ikeno, T. Sato, and A. Kamio: *Scripta Metall. Mater.*, 1995, vol. 32, 1175-80.
- M. Tamizifar and G.W. Lorimer: *Aluminum Alloys: Their Physical and Mechanical Properties*, Proc. 3rd Int. Conf. Aluminum, L. Arnberg, O. Lohne, E. Nes, and N. Ryum, eds., 1992, vol. 1, pp. 220-25.
- D.K. Chatterjee and K.M. Entwistle: *J. Inst. Met.*, 1973, vol. 101, pp. 53-59.
- R.J. Livak: *Metall. Trans. A*, 1982, vol. 13A, pp. 1318-21.
- H. Suzuki, M. Kanno, and G. Itoh: *J. Jpn. Inst. Light Met.*, 1980, vol. 30, pp. 606-16.
- T. Sakurai and T. Eto: *Aluminum Alloys: Their Physical and Mechanical Properties*, Proc. 3rd Int. Conf. on Aluminum Alloys, L. Arnberg, O. Lohne, E. Nes, and N. Ryum, eds., Norwegian Institute of Technology and SINTEF Metallurgy, Trondheim, 1992, vol. 1, pp. 208-13.
- D.J. Chakrabarti, B.K. Cheong, and D.E. Laughlin: in *Automotive Alloys II*, S.K. Das, ed., TMS, Warrendale, PA, 1998, pp. 27-44.
- J.M. Silcock, T.J. Heal, and H.K. Hardy: *J. Inst. Met.*, 1953-54, vol. 82, pp. 239-48.
- P. Villars and L.D. Calvert: *Pearson's Handbook of Crystallographic Data for Intermetallic Phases*, 2nd ed., ASM, Metals Park, OH, 1991, vol. 1, p. 769.
- A.K. Gupta, P.H. Marois, and D.J. Lloyd: *Mater. Sci. Forum*, 1996, vols. 217-222, pp. 801-08.
- J.D. Bryant: *Automotive Alloys*, S.K. Das and G.J. Kipouros, eds., TMS, Warrendale, PA, 1997, pp. 19-36.
- D.W. Pashley, J.W. Rhodes, and A. Sendorek: *J. Inst. Met.*, 1966, vol. 94, pp. 41-49.
- L. Zhen and S.B. Kang: *Scripta Mater.*, 1997, vol. 36, pp. 1089-94.
- R.C. Dorward: *Metall. Trans.*, 1973, vol. 4, pp. 507-12.
- W.F. Miao and D.E. Laughlin: *Scripta Mater.*, 1999, vol. 40, pp. 873-78.
- S.D. Dumolt, D.E. Laughlin, and J.C. Williams: *Scripta Metall.*, 1984, vol. 18, pp. 1347-50.
- B. Jansson, M. Schalin, M. Selleby, and B. Sundman: *Computer Software in Chemical and Extractive Metallurgy*, Proc. 2nd Int. Symp., C.W. Bale and G.A. Irons, eds., 1993, pp. 57-71.
- W.F. Miao and D.E. Laughlin: Carnegie Mellon University, Pittsburgh, PA, unpublished research, 1999.
- K. Matsuda, T. Yoshida, H. Gamada, K. Fujii, Y. Uetani, T. Sato, A. Kamio, and S. Ikeno: *J. Jpn. Inst. Met.*, 1998, vol. 62, pp. 133-39.
- G. Thomas: *J. Inst. Met.*, 1961-62, vol. 90, pp. 57-63.
- M. Murayama, K. Hono, W.F. Miao, and D.E. Laughlin: National Research Institute for Metals, Tsukuba, Japan, unpublished research, 1999.
- G.A. Edwards, G.L. Dunlop, and M.J. Couper: *Proc. 4th Int. Conf. on Aluminum Alloys*, T.H. Sanders and E.A. Starke, eds., Georgia Institute of Technology, Atlanta, GA, 1994, pp. 620-27.
- L. Sagalowicz, G. Hug, D. Bechet, P. Sainfort, and G. Lapasset: *Proc. 4th Int. Conf. on Aluminum Alloys*, T.H. Sanders and E.A. Starke, eds., Georgia Institute of Technology, Atlanta, GA, 1994, pp. 636-43.
- H. Suzuki, M. Kanno, Y. Shiraishi, and K. Hanawa: *J. Jpn. Inst. Light Met.*, 1979, vol. 29, pp. 575-81.
- M. Tamizifar and G.W. Lorimer: *Aluminum Alloys: Their Physical and Mechanical Properties*, Proc. 3rd Int. Conf. on Aluminum Alloys, L. Arnberg, O. Lohne, E. Nes, and N. Ryum eds., Norwegian Institute of Technology and SINTEF Metallurgy, Trondheim, 1992, vol. 1, pp. 220-25.
- M. Saga, Y. Sasaki, M. Kikuchi, Z. Yan, and M. Matsuo: *Mater. Sci. Forum*, 1996, vols. 217-222, pp. 821-26.
- C. Panseri and T. Federighi: *J. Inst. Met.*, 1966, vol. 94, pp. 99-107.